Contents lists available at ScienceDirect

Materials Characterization

journal homepage: www.elsevier.com/locate/matchar

Data availability

Links listed below are the data deposition URLs from Data availability section. Please verify the links are valid. This page will not appear in the article PDF file or print. They are displayed in the proof pdf for review purpose only.

https://doi.org/10.18434/mds2-3876 Dataset Link: https://doi.org/10.18434/mds2-3876

Contents lists available at ScienceDirect

Materials Characterization

journal homepage: www.elsevier.com/locate/matchar

Highlights

Accelerating in situ X-ray tomography using sparse projections and deep learning

Materials Characterization xxx (xxxx) xxx

Nathan S. Johnson*, Orion L. Kafka, Newell Moser

- Demonstrated a reconstruction method enabling rapid, high-quality in situ X-ray tomography.
- Applied to Inconel tensile tests, increasing sampling density from 4 to 16 CT scans per experiment.
- Validated X-ray tomography results with follow up electron microscopy; correlated fracture surface features to in situ observations.
- Enabled direct observation of dynamic deformation mechanisms such as pore growth, coalescence, and shear banding.
- Provides a detector-agnostic, self-supervised framework that bridges the performance gap between laboratory and synchrotron XCT.

Contents lists available at ScienceDirect

Materials Characterization

journal homepage: www.elsevier.com/locate/matchar

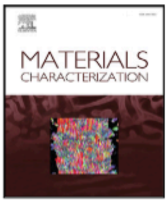

Accelerating in situ X-ray tomography using sparse projections and deep learning

Nathan S. Johnson [a],*, Orion L. Kafka [b],[1], Newell Moser [b]

[a] Carl Zeiss Research Microscopy Solutions, 5300 Central Parkway, Dublin, CA 94568, United States of America
[b] National Institute of Standards and Technology, Applied Chemicals and Materials Division, 325 Broadway, Boulder, CO 80305, United States of America

ARTICLE INFO

Dataset link: https://doi.org/10.18434/mds2-3876

Keywords:
Materials science
Deep learning
In situ
X-ray microscopy
X-ray tomography
Electron microscopy
Fractography
Mechanical properties
High throughput
Additive manufacturing
Inconel

ABSTRACT

In situ X-ray tomography experiments provide powerful insight into material deformation and damage evolution under mechanical load. However, laboratory-based tomography instruments often suffer from long acquisition times that limit temporal resolution. In this work, we evaluate a deep-learning-based reconstruction method capable of producing high-quality volume reconstructions from sparse (10x fewer) projection datasets. We apply this approach to in situ tensile experiments on additively manufactured Inconel 718 dog-bone specimens, increasing sampling density from a few tomography scans per experiment to over 20 scans at different load steps. We compare conventional Feldkamp–Davis–Kress (FDK) reconstructions using 1001 projections with both (a) FDK reconstructions using 101 projections and (b) deep-learning reconstructions using 101 projections. Qualitative and quantitative comparisons between reconstructions show that the deep-learning approach reduces noise and preserves major structural features, enabling reliable tracking of pore evolution during deformation. However, differences in intensity distributions and boundary smoothing introduced by the deep learning reconstruction influence segmentation results, particularly for small and intermediate pore sizes. These effects lead to differences in pore size distributions compared to traditional reconstructions. The deep-learning workflow substantially increases temporal resolution, enabling observation of deformation mechanisms such as pore growth, coalescence, and shear band formation that would otherwise be difficult to capture. These results demonstrate that deep-learning-enabled sparse acquisition provides a practical approach for accelerating laboratory in situ XCT experiments, particularly for studies focused on feature tracking and qualitative defect evolution.

1. Introduction

X-ray computed tomography (XCT) is a cornerstone of three-dimensional, non-destructive characterization across disciplines ranging from rock mechanics and battery science to structural composites and biomaterials. When combined with *in situ* stimuli—mechanical load, temperature, fluid flow, or chemical attack—XCT reveals the real-time evolution of internal features such as pores, cracks, or phase boundaries, enabling mechanistic insight that is inaccessible to surface techniques [1,2].

Among the most compelling applications is the study of additively manufactured (AM) alloys, where process-induced defects strongly influence performance. Synchrotron *in situ* XCT has clarified how pore morphology and heat-treatment dictate failure in AM stainless steel [3], and has quantified pore shape changes in directed-energy-deposited Inconel 718 during monotonic tension [4]. Similar approaches have illuminated ductility loss in wire-arc AM aluminium [5] and high-temperature damage in laser powder bed fusion (L-PBF) Invar 36 [6]. Work by Samei in AlsiMg [7], CuSn [8], and AZ31 [9] have clearly elucidated the benefits of in situ XCT. Samei's studies were able to closely track the shape evolution of defects during loading, showing behaviors such as pore migration to the surface, crack initiation, and void nucleation [7–9]. Through these observations, researchers were able to link the composition and processing parameters back to the mechanical behavior [9]. These studies underscore the power of time-resolved 3-D imaging for linking microstructure to mechanical response in AM components.

Synchrotron facilities require only millisecond exposure times thanks to high flux and fast CMOS detectors; some facilities have demonstrated continuous acquisition for in-situ studies ranging from 20 Hz rates [1], to sub-millisecond [10,11] and up to near-real-time

---

* Corresponding author.
E-mail address: nathan.johnson@zeiss.com (N.S. Johnson).
[1] Currently at QuesTek Innovations, LLC.

https://doi.org/10.1016/j.matchar.2026.116524
Received 25 August 2025; Received in revised form 4 May 2026; Accepted 16 May 2026

imaging [12]. In contrast, laboratory-based XCT systems typically require hundreds to thousands of projections with seconds-long exposures, stretching a single scan to tens of minutes. The need to pause loading during each scan limits temporal resolution and can introduce artefacts from stress relaxation or drift. High-resolution scintillator-coupled detectors exacerbate the trade-off between speed and magnification due to long refresh times, whereas flat high-refresh rate detectors sacrifice spatial resolution.

Low temporal resolution makes many analysis tasks more difficult. In AM, 4D deformation datasets are commonly paired with Digital Volume Correlation (DVC) [13,14] or defect tracking/evolution studies [5]. A primary challenge for all of these quantification approaches is registering datasets across time steps. Deformation and movement of the material makes registration a non trivial task. When 4D datasets have low temporal resolution there can be major changes in the sample between datasets, making registration even more difficult. This has led to the creation of many robust registration methods [15,16]. It has also generated some non-traditional acquisition techniques, such as relying on X-ray radiography instead of full tomography [13,17].

Acquiring many tomographies at a high rate makes the problem more tractable because sample changes are minor from step to step. It also enriches material modeling from the 4D dataset; high temporal density requires less interpolation between time steps. The long acquisition times associated with laboratory XCT prevent collecting tomographies at a high rate.

To mitigate these constraints, researchers have explored hardware and algorithmic solutions. On the hardware side, continuous-rotation stages and fast flat-panel detectors shorten cycle time but constrain optical magnification [18]. Algorithmically, iterative and model-based reconstructions that incorporate computer-aided design (CAD) priors recover volumes from tens of projections [19,20]. Reconstruction from sparse, ‘golden angle’ tomographies has been a long-used approach to retain reconstruction quality while reducing scan time [21]. More recently, deep-learning (DL) approaches — including noise2noise [22] and just-in-time neural reconstruction — have produced high-quality reconstructions from sparse projection sets at synchrotrons and, to a limited extent, in the lab [2,23]. In specific cases, researchers have been able to perform full 4D reconstructions from just two projections at each time step [24].

Here we test a general DL reconstruction framework, *DeepRecon* [23], that overcomes two key limitations of existing methods: (i) it requires no pre-training on external datasets and instead learns directly from a single full-projection scan of the specimen under study, and (ii) it is detector-agnostic, operating equally well with high-speed flat detectors and high-resolution objective-coupled detectors. Applying *DeepRecon* to laboratory *in situ* tension tests on laser-powder-bed-fused Inconel 718, we reduce the projection count by an order of magnitude (1001 → 101) and the scan time from approximately 45 min to approximately 8 min per load step. This allows us to capture 16 tomographies during a single tensile experiment, compared to 4 tomographies collected in the same amount of time previously. This is all done while preserving segmentation fidelity for pore tracking.

The remainder of the paper details the experimental setup (Section 2), evaluates reconstruction and segmentation quality (Section 3), and discusses implications for high-throughput 4-D characterization of AM metals (Section 4).

2. Materials and methods

2.1. Sample preparation and setup

Table 1
Manufacturing parameters for laser powder bed fusion manufacturing of the dogbone specimen.

Laser Power (W)	Scan Speed (mm/s)	Layer thickness(μm)	Build orientation (°)	Laser energy density (J/mm^2)
330	1770	30	0	62

Dog-bone tensile coupons of Inconel 718 were fabricated by LPBF on a *EOS M290*[2] system equipped with a 330 W Yb-fiber laser, lasing with nominal volumetric energy density of 62 $\mathrm{J\,mm^{-2}}$ (Table 1). Spherical IN718 powder, supplied by 3D Systems and recycled to 3D Systems' usability standards, was spread in 30 μm layers under a flowing argon atmosphere [25]. Coupons were built with their gauge axis vertical (z direction), i.e., parallel to the build direction, to minimize anisotropy. They were cut using wire electrical discharge machining from the grip section of larger fatigue coupons built for a previous study [25]. The coupon geometry is the same as that used in [17], with a 0.7 mm by 0.3 mm gauge cross-section and 2 mm gauge length.

Each coupon was prescreened in a ZEISS Xradia Versa 630 using a 4× objective at 3.950(146) μm/px (see Table 2). A simple global Otsu threshold identified pores larger than 5 voxels. We selected a specimen exhibiting an initial porosity fraction of 0.051(1) % to ensure sufficient internal features for defect-tracking validation.

Coupons were mounted in a Deben CT5000 [26] micro-tensile stage using custom titanium grips and aligned optically to keep the gauge volume centered in the 4 mm field-of-view during rotation. The X-ray source was pushed as close to the Deben stage as possible without collision to maximize X-ray flux and image intensity. The detector was positioned to balance the field of view with pixel resolution. The final detector position was chosen such that the entire sample gauge was in the field of view, but nothing more. As displacement was applied, the bottom portion of the gauge moved out of view, while the top portion remained fixed.

2.2. Data collection

2.2.1. Mechanical loading

Tensile tests were conducted in a Deben CT5000 micro-tensile stage equipped with a 5 kN load cell. The gauge region was aligned vertically and centered within the X-ray field-of-view. Loading was displacement-controlled at 0.10 mm/min or 3.3×10^{-3} /s nominal strain rate. After a 10 N preload, the specimen was pulled in 25 μm increments up to the onset of plasticity; beyond that point, step size increased to 100 μm. Immediately after each displacement increment the cross-head was stopped and a tomography acquired.

A comparison between the traditional in situ workflow and the deep-learning based workflow can be seen in Fig. 1a. One high projection density (1001 projections) scan at 10 N served as the training input for the deep learning model. Thereafter, a total of 16 sparse-projection (SP) scans (101 projections) were collected at successive load steps. Additional high density scans (1001 projections) were collected at crosshead displacements of 30 μm and 250 μm, or crosshead strains of 0.14% and 2.37% respectively. The additional HD scans were reconstructed using the Feldkamp-Davis-Kress (FDK) algorithm [27] and used for validation of segmentation results.

Fig. 1c plots the force–displacement history; periodic force drops coincide with tomography pauses, during which the specimen relaxed elastically. At later displacement steps (after 425 μm) the sample was loaded in increments of 25 μm to prevent breakage; once significant plasticity had been observed (at 750 μm) a penultimate tomography was taken, along with a final tomography after fracture at 800 μm.

---

[2] Certain commercial equipment, instruments, or materials are identified in this paper in order to specify the experimental procedure adequately. Such identification is not intended to imply recommendation or endorsement by NIST, nor is it intended to imply that the materials or equipment identified are necessarily the best available for the purpose.

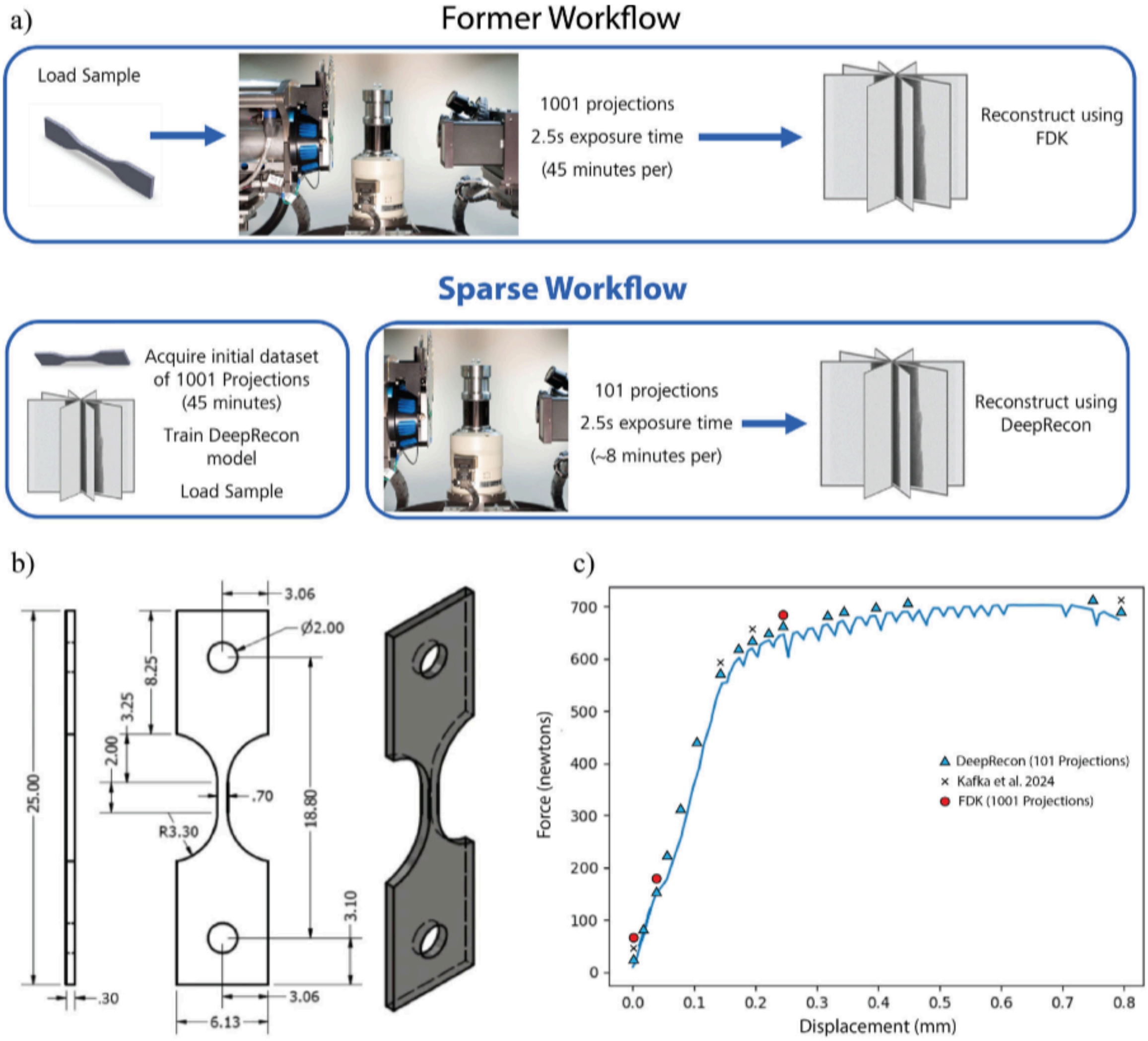

Fig. 1. (a) Overview of the traditional workflow (top) compared to the sparse, deep-learning based workflow. (b) Dogbone geometry for the samples used in this study. Image reproduced with permission from Kafka et al. [17]. Dimensions in mm. (c) Force–displacement curve for the sample studied.

2.2.2. *X-ray and electron microscopy*

X-ray imaging was performed on a ZEISS Xradia 630 Versa X-ray microscope. Key parameters are summarized in Table 2. Briefly, scans used a 140 kV, 21 W polychromatic beam filtered with the ZEISS HE2 filter. A 4 × scintillator-coupled objective produced an effective voxel size of 3.9512 μm. Each projection was exposed for 2 s and digitized at 32 bit. Scans covered 360° rotation with an angular step of 0.36°. Raw projection sets were archived in 32-bit TIFF format. After reconstruction (Section 2.3), volumes were exported as 3-D TIFF stacks for segmentation and pore-tracking analysis.

Scanning electron microscopy (SEM) was performed with a ZEISS Gemini 460 microscope. All images were acquired with secondary electron (SE) imaging. Additional metadata, including pixel size and scale bar, are included in the images.

2.3. *Deep-learning reconstruction*

Deep learning reconstruction was performed using the commercially available ZEISS DeepRecon Pro model within the ZEISS Advanced Reconstruction Toolbox (ART) version 4.0 [22,23,28,29]. DeepRecon Pro is a previously developed deep-learning reconstruction framework and is evaluated in this work; no modifications to the architecture or training procedure were performed.

Table 2
X-ray acquisition parameters for high-density (“HD”) and sparse (“SP”) scans.

Parameter	HD scan	SP scan
Projections (N)	1001	101
Exposure time per proj. (s)	2	2
Total scan time (min)	≈45	≈8
Rotation range (°)	Full 360	Full 360
Angular step (°)	0.36	3.6
Source power (W)	21	21
Source voltage (kV)	160	160
Pixel size (μm)	3.9512	3.9512
Source-Sample Distance (mm)	70	70
Sample-Detector Distance (mm)	334	334
Filter	HE2	HE2
Optical Magnification	4X	4X
Binning	2	2
Adaptive Motion Compensation	No	No

The DeepRecon approach is based on a self-supervised noise-to-noise convolutional neural network framework [22,23,28]. A full-projection dataset (1001 projections) was first acquired and used for model training. The projection dataset was internally split into training pairs to estimate noise characteristics and train the model to suppress

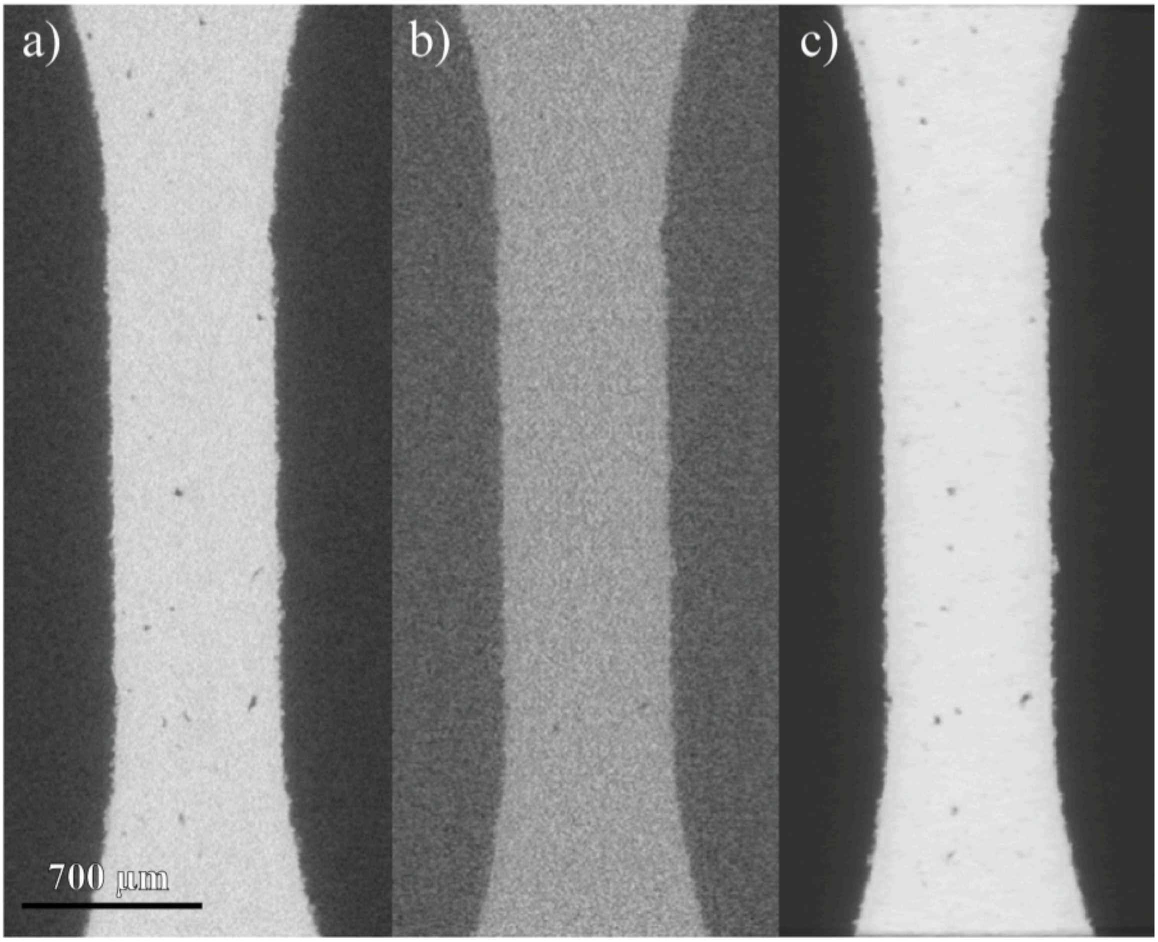

Fig. 2. Comparison of reconstruction results at 0 µm displacement step using (a) the FDK algorithm and 1001 projections, (b) the FDK algorithm and 101 projections, (c) deep learning reconstruction and 101 projections.

noise and improve reconstruction quality. Once trained, the model was applied to sparse-projection datasets (101 projections) collected at subsequent load steps.

The reconstruction model is based on a U-Net-like convolutional neural network architecture that operates on 3D volumes using a 2.5D approach. The network processes volumetric tiles of 512 × 512 × 5 voxels and consists of three primary components: a contracting path, an expanding path, and skip connections. The contracting path contains convolutional and pooling layers that extract hierarchical features, while the expanding path performs upsampling and feature reconstruction. Skip connections preserve spatial information and improve reconstruction fidelity. Additional convolutional layers refine the reconstructed output and enhance feature recovery [23].

A full density 1001 projection dataset is used for model training. The initial projection dataset is split into testing and training pairs that are used to estimate the noise level in the data. Training is performed using the Adam optimizer with a learning rate of 0.0002, batch size of 8, and approximately 10,000 training iterations. The model is trained to reduce noise and enhance contrast in the images. Once the model is trained, it is used to produce the de-noised 3D reconstructed volume. Reconstructions were performed in the proprietary Scout and Scan Reconstructor platform [30] using the proprietary ZEISS Advanced Reconstruction Toolbox (ART) version 4.0.

Training was performed on a GPU (Nvidia RTX4090). Training time was approximately 1 h and 45 min, while inference for each sparse-projection dataset required approximately 5 min. Reconstructed volumes were exported as 32-bit floating-point TIFF stacks (3.89 µm voxel size) and passed to the segmentation pipeline described in Section 2.4.

To evaluate reconstruction fidelity, deep learning reconstructions were compared to full-projection FDK reconstructions using structural similarity index measure (SSIM) [31], intensity histogram comparisons, and segmentation-based pore analysis.

Because DeepRecon Pro is a commercially available proprietary tool, internal training metrics such as gradient evolution, loss convergence curves, and additional hyperparameter settings are not accessible to the user. However, architecture and training details are documented in prior publications and vendor documentation [32].

2.4. Segmentation, registration, and pore tracking

All image analysis was performed in Python 3.11 (Anaconda distribution) using `imppy3d` v1.2.3 [33], `SimpleITK` v2.3.1 [34–36], `scikit-image` v0.23 [37], and `numpy` v1.26 [38]. The complete segmentation pipeline and Conda `environment.yml` is available in the supplementary materials.

A global Otsu threshold [39] (T_{Otsu}) was computed on the initial load step to segment the sample and internal pores. This threshold was then used for segmentation of all subsequent volumes. Voxels with gray value < T_{Otsu} were labeled “pore”. Binary volumes were cleaned by a 3-D morphological opening (radius 1 voxel) followed by removal of connected components smaller than 27 voxels (equivalent to a spherical pore of diameter 11.8 µm). Successive volumes were registered to the zero-load DL reconstruction using a rigid transform in `SimpleITK`. Optimization employed Pearson’s correlation coefficient, a gradient-descent step size of 0.5 voxel, and a convergence tolerance of 1×10^{-8}. w

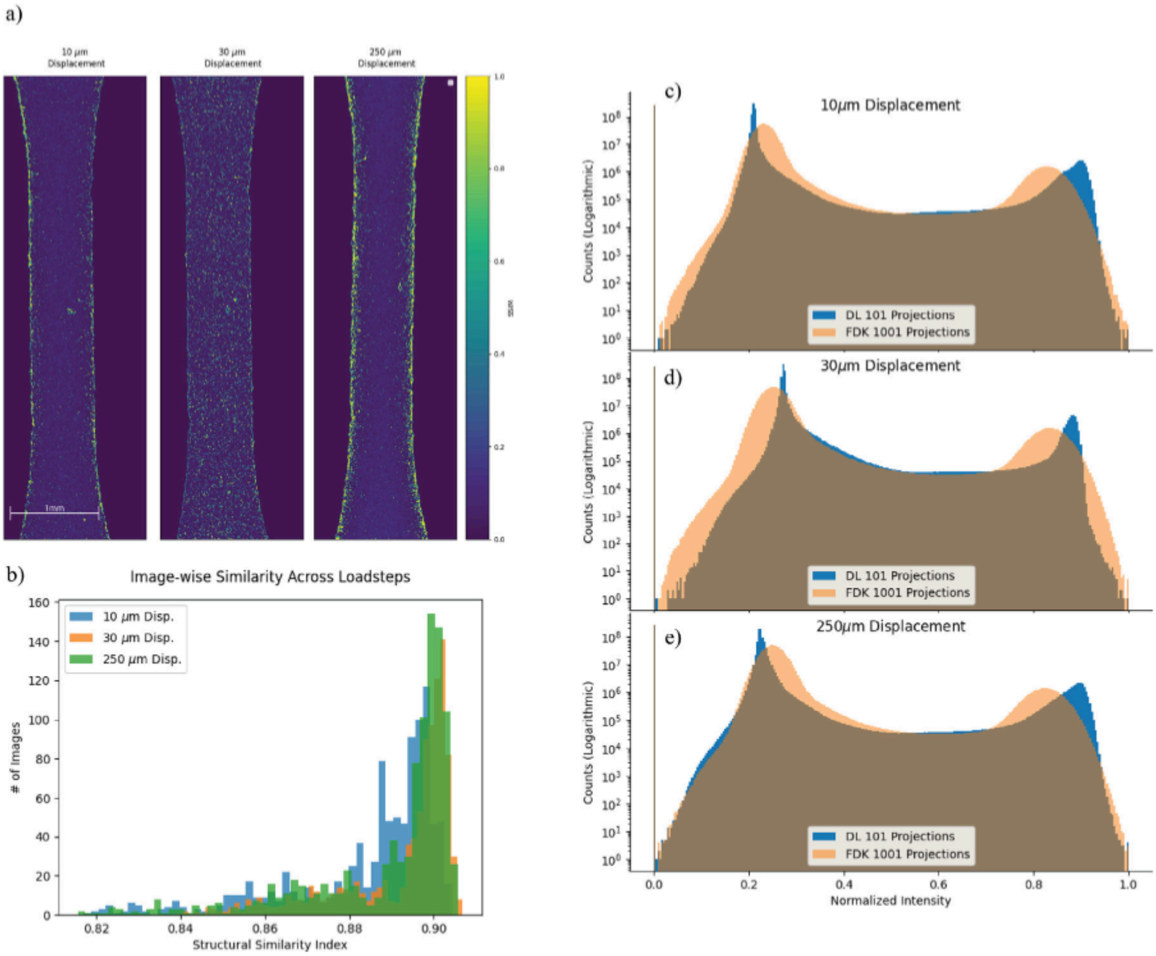

Fig. 3. Comparison between FDK and DL reconstructed volumes. (a) Pixel-wise SSIM at slice z=133 through the sample for the three loadsteps with FDK reconstructions. (b) SSIM measured inside the sample region for three loadsteps. (c–e) Intensity histograms for DL (blue) and FDK (orange) reconstructions at the 10 μm, 30 μm, and 250 μm displacement steps.

3. Results

3.1. Raw reconstruction and mechanical results

A comparison of the same 2D slice through the sample under various reconstructions can be seen in Fig. 2. The standard FDK reconstruction with 1001 projections at 10 N load can be seen in Fig. 2a. When reconstructed using only 101 projections and the FDK algorithm, as shown in Fig. 2b, the noise increases significantly and internal features become obscured. Some of the largest pores in the slice can still be observed in the FDK 101 projection reconstruction, but all medium and small pores are lost to the increased signal-to-noise ratio. By comparison, the DL reconstruction, on the right in Fig. 2, demonstrates decreased noise in both the air and the Inconel, while retaining the contrast necessary to measure the smallest pores. The filters used in the DL reconstruction do cause some blurring at the boundaries of features. Close inspection of the samples' internal pores show slight distortion at the edge. This will impact the sample segmentation, as discussed later.

Fig. 3 provides more in depth analysis of differences between the FDK and DL reconstructions. Fig. 3a shows the difference between the FDK and DL reconstructions (for a single slice of the volume). The difference was computed as $(\text{Image}_{\text{FDK}} - \text{Image}_{\text{DL}})/\max(\text{Image}_{\text{FDK}})$. The vast majority of the difference inside the sample are single pixels with slightly different intensity values due to speckle noise. For the 10 μm and 250 μm displacement steps, there are some larger differences at the edge of the sample and at the edge of pores. These regions are only a few pixels in width total.

The SSIM was also computed for the reconstructed volumes. Each slice in the DL and FDK reconstructions were compared against each other using the SSIM, as shown in Fig. 3b. The majority of images had a similarity value near 0.9 The worst matching images had an SSIM as low as 0.8.

The image intensity histograms in Fig. 3 reveal where some of the differences between the reconstructions arise. The DL reconstruction tends to sharpen intensity peaks by removing the speckle noise, while also pushing these peaks toward slightly high values. The peak shift arises from the enhanced contrast of the DL reconstruction.

3.2. Segmentation results

A 2D segmentation comparison looking down the gauge can be seen in Fig. 4. The top most images (a and b) show the reconstructed slice, while the middle images (c and d) show the segmented sample, and the bottom images (e and f) show the segmented internal porosity. The areas highlighted by boxes show pores that demonstrate significant differences in size between the FDK and DL reconstructions. Blurring can occur in the DL reconstruction that slightly erodes the edges of pores. For the smallest pores, this can mean that the pore is entirely lost in the DL segmentation. For mid-sized pores, while the pore is still present enough to be segmented, the segmented volume trends lower compared to the FDK segmented pores due to the eroded edges. For the largest pores, differences between the FDK and DL reconstructions are only a few pixels in size. The only noticeable difference is that regions

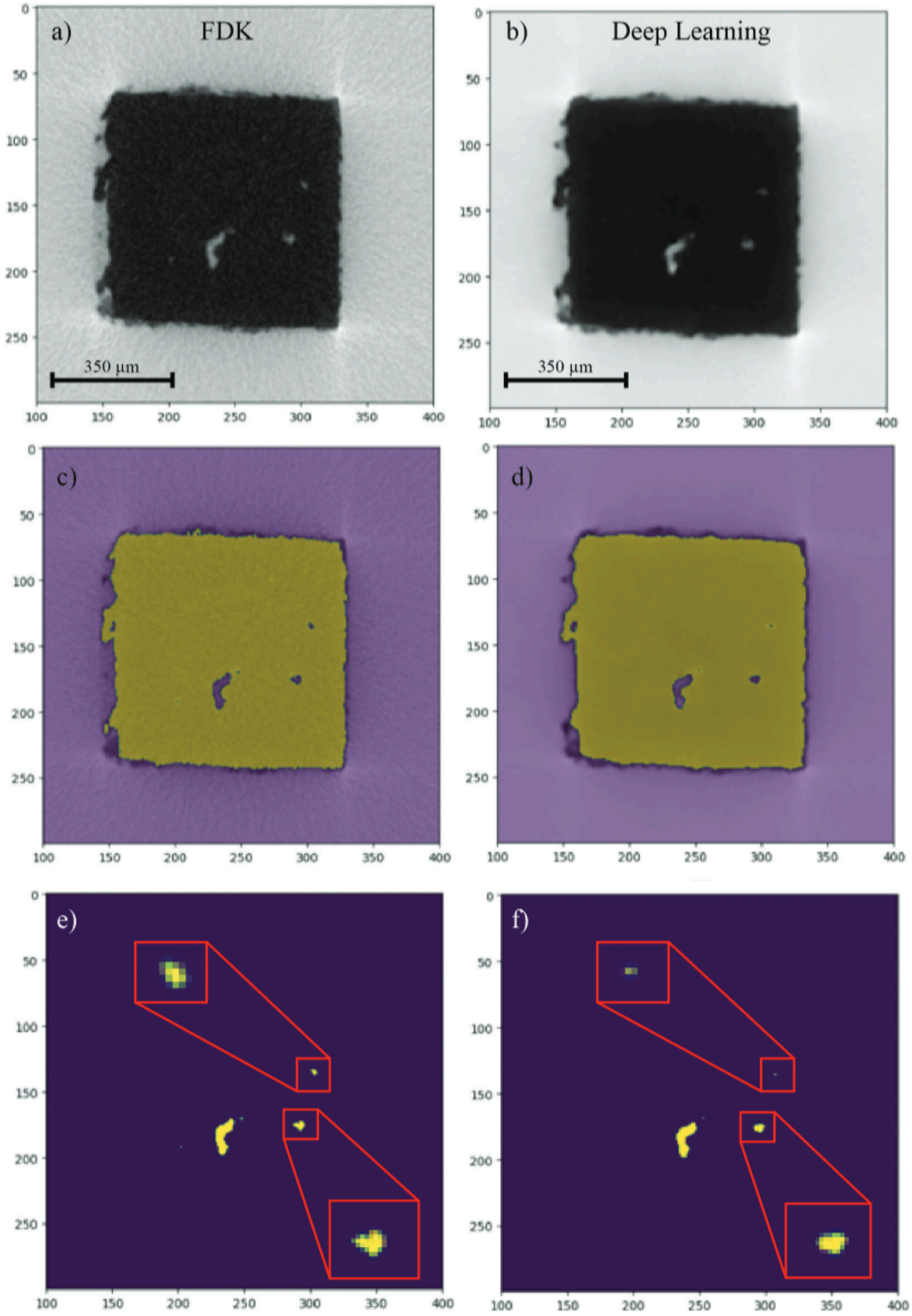

Fig. 4. A comparison of segmentation results between FDK and deep learning reconstructions. (a) 2D slice of an FDK reconstruction with 1001 projections. (b) 2D slice of a DL reconstruction with 101 projections. (c) Segmentation of the sample from FDK reconstruction. (d) Segmentation of the sample from DL reconstruction. (e) Segmentation of porosity from FDK reconstruction. (e) Segmentation of porosity from DL reconstruction. Red boxes in (e) and (f) are meant to highlight pores that are distorted between the FDK and DL reconstructions.

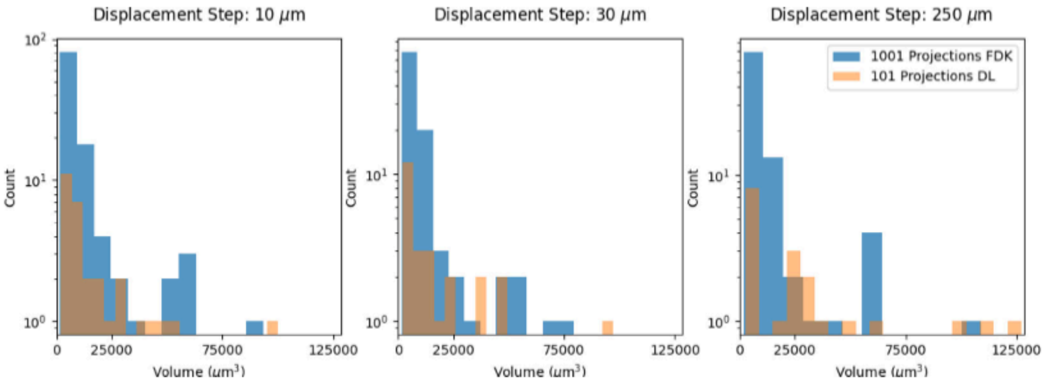

Fig. 5. A histogram comparison of pore volumes between FDK 1001 projection reconstruction (blue) and DL 101 projection reconstruction (orange) at displacement steps (a) 10 µm, (b) 50 µm and (c) 250 µm.

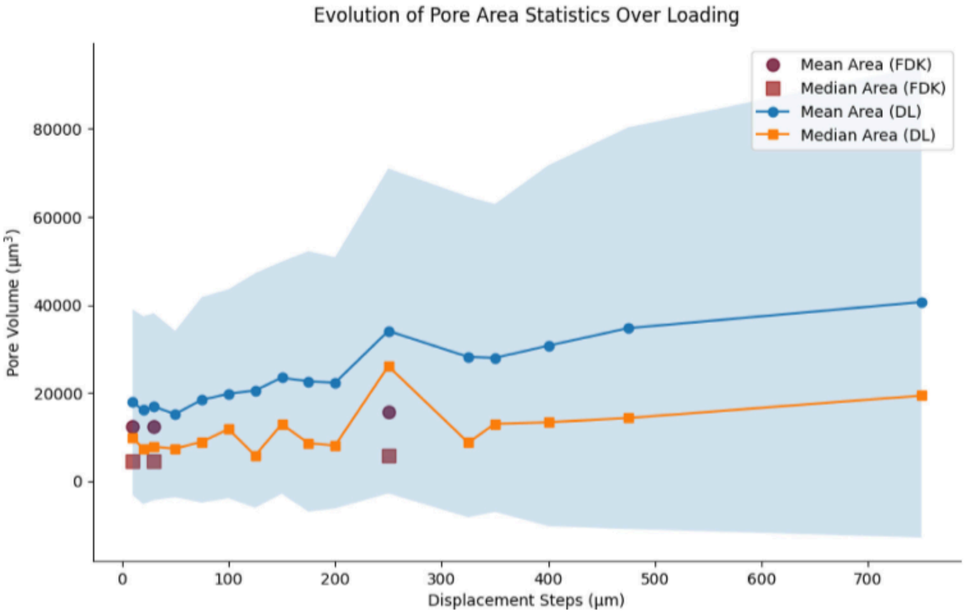

Fig. 6. The evolution of pore volume across displacement steps. Blue and orange dots represent the mean and median pore volume, respectively, for the DL reconstruction. Red circles and squares are the median and mean pore volume, respectively, for the FDK reconstruction. Blue shading indicates ±1 standard deviation away from the mean at each step.

of high curvature on the edge of the pore can be slightly distorted, again due to blurring.

The qualitative segmentation results shown in Fig. 4 are backed up by quantitatives comparison shown in Fig. 5 & 6. A histogram comparison of the DL reconstructions and full 1001 FDK reconstructions at displacement steps 10 µm, 30 µm and 250 µm are shown in this figure, reinforcing that the FDK segmentation produces many smaller pores. The larger pores in the FDK reconstruction tend to be smaller than their counterparts in the DL reconstruction, again due to blurring at the edge that causes the DL segmentation to bleed outward into the sample region.

A statistical view of the pore evolution as load increase is shown in Fig. 6. The *y*-axis shows the mean/median volume of segmented pores across each load step on the *x*-axis. The three load steps that were collected with 1001 projections and reconstructed using the FDK algorithm are shown in red. The previous qualitative and quantitative results shown in Figs. 2 & 5 are repeated here; the mean and median FDK reconstructions tend much closer to smaller values owing to the presence of small voids in the FDK segmentation. The difference between the median DL and FDK reconstructions is small at load-steps 10 µm, 30 µm, and 250 µm. The mean values have a much larger difference because the mean is more strongly affected by biases and outliers.

The behavior of the mean/median pore volume across loading in the DL reconstructions (blue/orange markers respectively) is as expected: the pore volume increased with increasing tensile load. There is some variation in the pore volume across load steps especially in the early displacement region. This is likely due to the aforementioned relaxation that occurs while the sample is held statically for tomography.

Fig. 7 shows a comparison between FDK and DL segmentation results for one of the largest pores. For every dataset compared, the segmented pore areas are within a few pixels of each other. However, it can be clearly seen that there is a difference in shape between the segmented pores. Whereas FDK reconstructions tend to maintain sharp features, blurring filters used by the DL approach tend to round out internal porosity. This has implications for in situ studies that are quantifying pore shape and defect type.

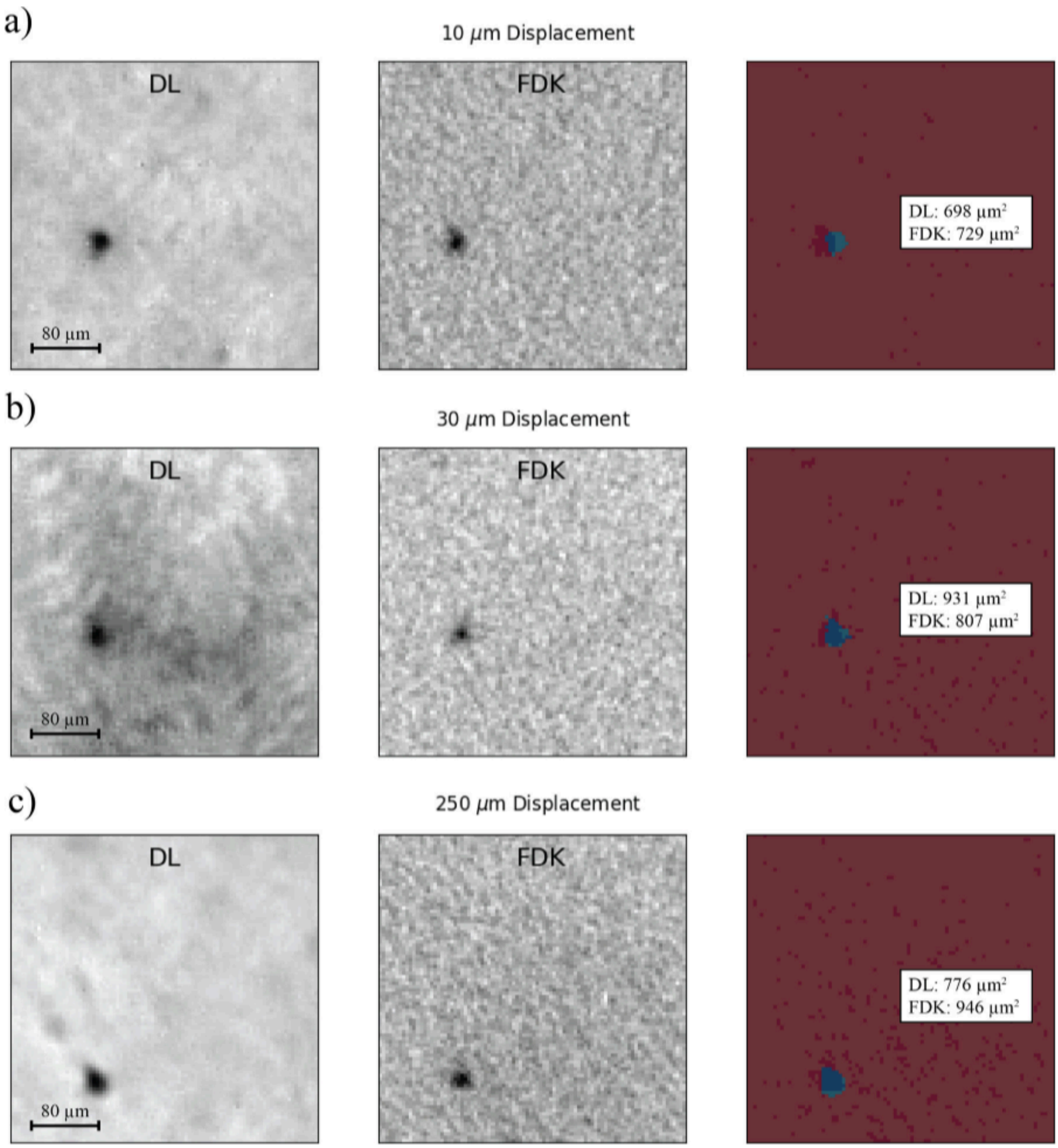

Fig. 7. Comparison of individual pore segmentations and their size. A slice through one of the largest pores is shown for the (a) 10 μm (b) 30 μm and (c) 250 μm displacement steps. Leftmost images are the deep learning reconstruction, middle images are the FDK reconstruction with 1001 projections, and the right hand size shows overlays of pore segmentations between the two volumes. The right hand images are labeled with the 2D pore area for the DL and FDK segmentations.

3.3. Fractography

SEM fractography was performed on both halves of the fractured sample; emphasis was placed on the upper half because it revealed more interesting features. Relevant fractography images of the upper half are shown in Fig. 8. Multiple failure modes were observed. The dominant failure mechanism was ductile fracture as evidenced by microvoid coalescence (Figs. 8a and c). Microvoid coalescence can be seen across almost the entire fracture surface. The fracture surface also appears to have permeated through (or originated at) this pore.

Striations are also apparent on the fracture surface, indicative of shear banding before failure. These striations are especially apparent in Figs. 8a and c. These striations correspond with a large internal pore, in the upper right hand side of 8a.

Intergranular and intragranular fracture is also observed at several sites. Intergranular fracture is most clear in Fig. 8a. Several grain boundaries can be observed by their flat faces that are devoid of microvoids. Intragranular fracture is evidenced in Fig. 8b. This image shows what appears to be a large inclusion particle sitting inside a void. The rough facets of the grain face indicate fracture occurred through the crystal, instead of at a boundary. All of the fracture behaviors observed are consistent with Inconel 718's known fracture mechanisms [40].

4. Discussion

4.1. Reduction of tomography acquisition time

Previous in situ studies on from the same build plate required 45 min of instrument time to collect 1001 projections [17]. The four tomography points acquired by Kafka et al. amounted to around 3 h of instrument time total [17]. In this experiment, we acquired an initial

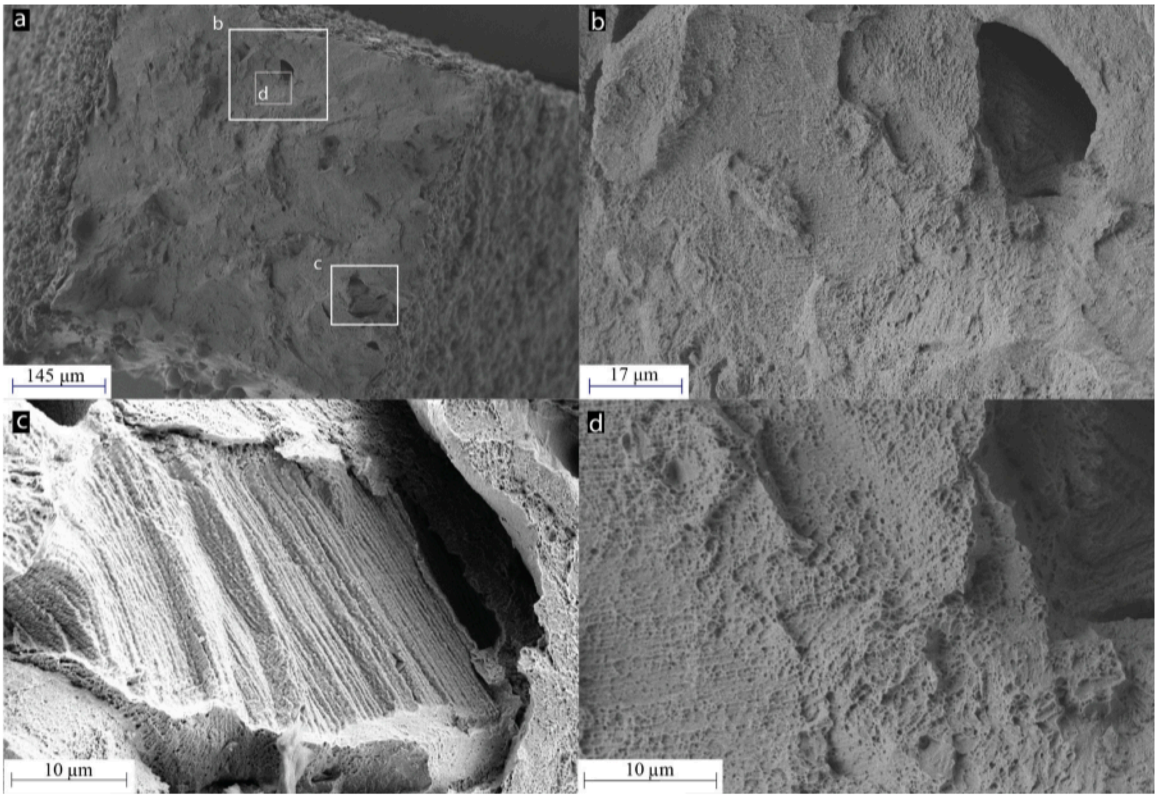

Fig. 8. SEM Fractography of the upper failure site. (a) Overview of the fracture surface from the lower sample half. (b) Fracture surface featuring a large internal pore, grain facets, and microvoid coalescence. (c) Large internal feature, possibly an inclusion, through the fracture surface. (d) Close-up view of microvoids and striations on the fracture surface.

dataset of 1001 projections to train the model (45 min). All subsequent tomographies were acquired with 8 min of instrument time to collect 101 projections. That is a 5x improvement in scan speed and a 10x reduction in data acquisition. Over the course of 3 h, we were able to acquire 16 tomographies in total, representing a 4x increase in sampling density over previous experiments.

This is a considerable increase in sampling density, especially for dynamic in situ experiments that may have features (like cracks) that suddenly appear. It is much easier to observe these features when acquiring many tomographies over the course of an in situ experiment. Furthermore, it enables even higher fidelity quantification than low density sampling, as described in the next section.

A key advantage is that the sample can be continuously loaded with minimal interruption, mitigating relaxation and slippage. Some slippage was observed (force drops without apparent fracture, shown in Fig. 1b), but overall, pore movement and coalescence were clearly visualized.

4.2. Analysis of pore segmentation

The success of pore segmentation from the DL reconstruction, compared to traditional FDK reconstruction, depends largely on the type of analysis being performed. Researchers typically need very accurate measurement of pore shapes [41], or they need to calculate how many pores are in the sample [42]. In many cases both analyses are required [20,43–45].

Figs. 5 & 6 demonstrate that the DL and FDK segmentations differ for small pores. Blurring by the DL reconstruction obfuscates some of the smaller pores. On the one hand, DL reconstruction removes speckle noise that may be segmented as a small ‘pore’ but is really just a few bright pixels. We can conclude that the DL segmentation contains fewer pores of smaller volume and that the size/shape of pores is slightly altered due to blurring. However, we must keep in mind the impact of the segmentation method used. Here, we used a simple thresholding segmentation. A more robust/complex segmentation approach, such as machine-learning or neural network based segmentation, may improve results. We cannot definitively say if the differences arise only because of the DL reconstruction, or the segmentation method used, or both.

In addition to differences observed in small pores, the deep learning reconstruction also alters the distribution of mid-sized pores, as shown in Fig. 5. These differences arise from two primary effects introduced by the deep learning reconstruction. First, the deep learning reconstruction modifies the intensity histogram of the reconstructed volumes, as shown in Figs. 3c–e. The reduction in speckle noise and increased contrast shift the grayscale distribution, which affects threshold-based segmentation.

Because the segmentation in this study was performed using an automated Otsu threshold, differences in intensity histograms lead to different segmentation thresholds between datasets. As a result, some pores may be slightly over-segmented or under-segmented when comparing deep learning and FDK reconstructions. This effect contributes to differences in the observed pore size distributions, including the absence of certain peaks in the deep learning distributions.

Second, the deep learning reconstruction introduces slight smoothing at pore boundaries, as illustrated in Figs. 4 and 7. These boundary modifications alter pore shapes and volumes. Even small changes in boundary definition can propagate into measurable differences in pore volume, particularly for mid-sized pores. Thus, segmentation differences are not limited to sub-voxel-scale features but may influence intermediate pore sizes as well.

These effects complicate one-to-one comparisons between segmentation results. In this study, we intentionally applied the same segmentation method (Otsu thresholding) to both datasets without manual tuning. An alternative approach would have been to adjust segmentation parameters to enforce agreement between distributions. However,

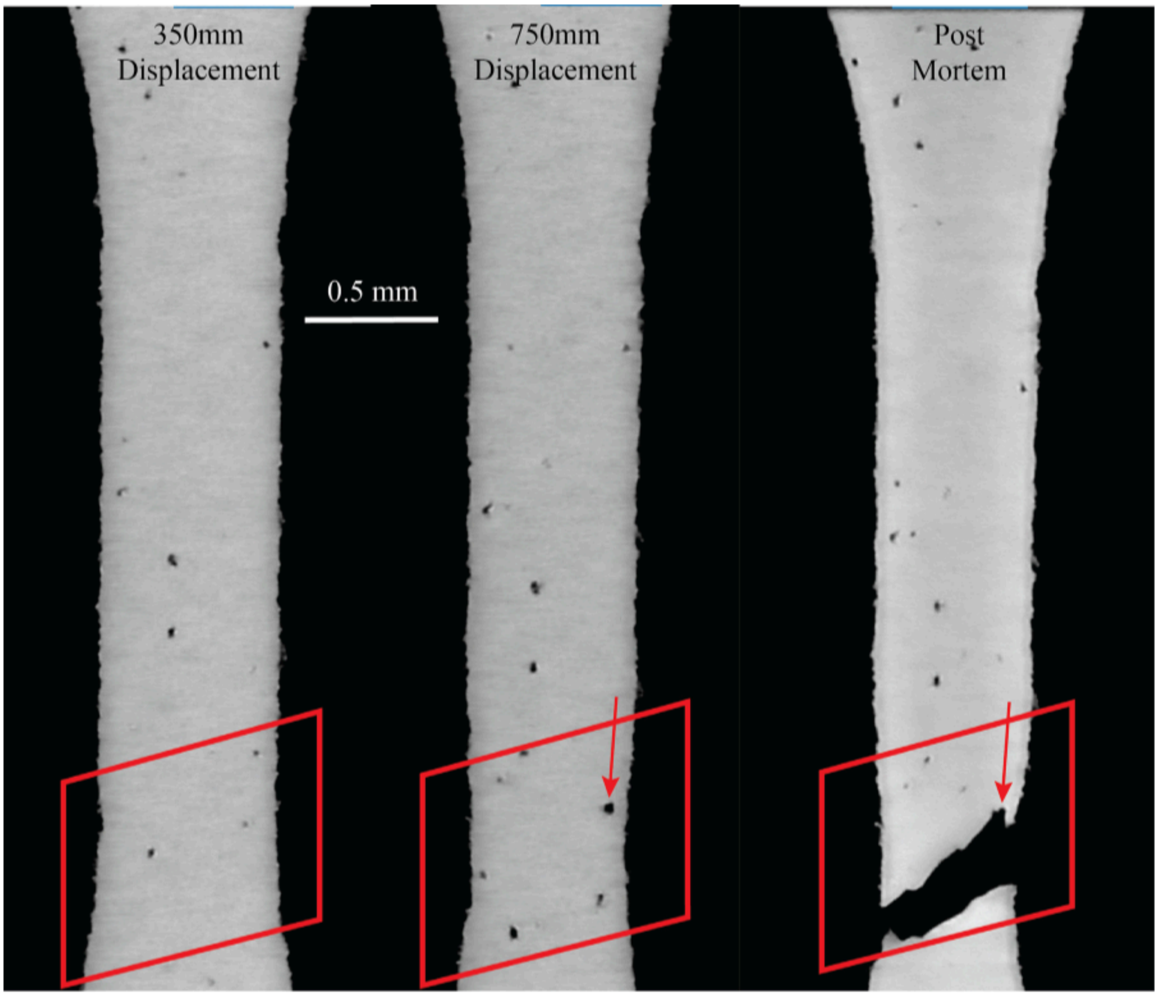

Fig. 9. The onset of shear banding during the final displacement steps. Fracture occurred across a pore, highlighted by the red arrow.

doing so would shift the focus of the study from evaluating reconstruction fidelity to evaluating segmentation tuning. Therefore, we elected to apply identical segmentation workflows and report the resulting differences directly.

These findings suggest that deep learning reconstruction is well-suited for tracking larger defects and observing qualitative trends in pore evolution, but caution should be exercised when interpreting absolute pore size distributions or when quantitative analysis of mid-sized features is required.

Users of deep learning reconstruction should walk away with this impression: segmentation of features from DL images match for the largest (easily distinguishable) features inside the sample. It may not be as reliable for segmentation of finer features near the pixel resolution of the dataset, especially when using the exact same segmentation method to compare results across FDK and DL reconstructed datasets.

4.3. Observation of shear banding

Some deformation mechanisms may not be observed during in situ experiments with too few acquisition points. Often, when tomographies are collected only at the beginning and end of an in situ experiment, it can be difficult to ascertain how exactly deformation occurred, where, and its impact on the mechanical properties. The benefit of taking many tomographies throughout an experiment is that these behaviors now become visible.

One example is seen in Fig. 9, where it appears that shear banding occurred inside the region shown in the red box. A portion of the sample edge appears to straighten out, a common indicator of a shear band. The fracture surface also cleaved through this region.

The follow-up fractography revealed a complicated fracture surface, as shown in Fig. 8. The pore highlighted in Fig. 9 is the same pore seen in Fig. 8b. The fracture surface cleaved through this pore or at its boundary. The rest of the fracture surface shows a combination of ductile fracture, evidenced by microvoid coalescence in Fig. 8d, and intragranular fracture, seen in Fig. 8b and c.

These complex deformation mechanisms were easily observed because deep learning reconstruction enabled many tomographies to be collected throughout loading. Traditionally, researchers would have to carefully observe the sample during loading to catch this kind of behavior and then choose to acquire a tomography at this load step.

5. Conclusion

This study demonstrates that a self-supervised deep-learning reconstruction strategy can unlock high-throughput *in situ* X-ray computed tomography on laboratory instruments for additively manufactured metals. Training *DeepRecon* directly on a single 1001-projection reference scan enabled faithful reconstruction of 101-projection tomographies acquired in ≈ 8 min—an order-of-magnitude reduction in scan time compared with conventional Feldkamp–Davis–Kress (FDK) reconstruction. The resulting dense time series (16 scans during monotonic tensile loading of LPBF Inconel 718) captured pore growth, coalescence, and final fracture with a temporal resolution to observe key features.

The methodology does have limitations. Deep learning reconstruction alters intensity distributions and introduces mild smoothing at feature boundaries, which can affect segmentation results. These effects propagate beyond sub-voxel-scale features and may influence intermediate pore sizes, particularly when threshold-based segmentation is used. As a result, absolute pore size distributions derived from deep learning reconstructions may differ from traditional reconstructions. However, larger defects and qualitative trends in pore evolution remain well preserved.

Extending the framework to cyclic loading, elevated temperatures, and other alloy systems will further establish deep-learning-enabled laboratory XCT as a routine tool for mechanistic studies of additively manufactured components.

In summary, the proposed deep-learning workflow provides a practical approach for accelerating laboratory in situ XCT experiments, particularly for studies focused on feature tracking, deformation evolution, and qualitative defect analysis. While differences in segmentation fidelity should be considered when interpreting absolute pore size distributions, the approach substantially increases temporal resolution and enables observation of deformation mechanisms that would otherwise be difficult to capture. These advantages make deep-learning-enabled sparse acquisition a valuable tool for many in situ XCT applications, though its applicability should be evaluated carefully depending on the quantitative requirements of a given study.

CRediT authorship contribution statement

Nathan S. Johnson: Writing – review & editing, Writing – original draft, Visualization, Validation, Supervision, Software, Resources, Project administration, Methodology, Investigation, Formal analysis, Data curation, Conceptualization. **Orion L. Kafka:** Writing – review & editing, Supervision, Resources, Investigation, Formal analysis, Conceptualization. **Newell Moser:** Writing – review & editing, Resources, Methodology, Investigation, Formal analysis, Conceptualization.

Generative AI Statement

The entire article draft was written by N.S. Johnson. Individual sections were checked for grammatical errors and typos using ChatGPT 4o (April 2025).

Declaration of competing interest

This research received no external financial or non-financial support. There are no additional relationships, patents, intellectual property, or additional activities to disclose.

Data availability

All data from this study including raw X-ray projections, reconstructed X-ray tomographies, and all Python scripts for data processing and figure creation are publicly available online at https://doi.org/10.18434/mds2-3876.

References

[1] E. Maire, C. Le Bourlot, J. Adrien, A. Mortensen, R. Mokso, 20 hz X-ray tomography during an in situ tensile test, Int. J. Fract. 200 (2016).

[2] A. Graas, S. Coban, K. Batenburg, F. Lucka, Just-in-time deep learning for real-time X-ray computed tomography, Sci. Rep. 16 (2023).

[3] H.D. Carlton, A. Haboub, G.F. Gallegos, D.Y. Parkinson, A.A. MacDowell, Damage evolution and failure mechanisms in additively manufactured stainless steel, Mater. Sci. Eng.: A 651 (2016) 406–414.

[4] O. Kafka, C. Yu, P. Cheng, S. Wolff, J. Bennett, E. Garboczi, J. Cao, X. Xiao, L. W.K., X-ray computed tomography analysis of pore deformation in IN718 made with directed energy deposition via in-situ tensile testing, Int. J. Solids Struct. 256 (2022).

[5] Z. Runyu, W. Li, Y. Jiao, C. Paniagua, Y. Ren, H. Lu, Porosity evolution under increasing tension in wire-arc additively manufactured aluminum using in-situ micro-computed tomography and convolutional neural network, Scr. Mater. 225.

[6] Q. Yang, K. Wei, Z. Qu, X. Yang, D. Fang, In-situ X-ray computed tomography of high-temperature tensile behavior for laser powder bed fused invar 36 alloy, Addit. Manuf. 83 (2024) 104072.

[7] J. Samei, M. Amirmaleki, M. Shirinzadeh Dastgiri, C. Marinelli, D.E. Green, In-situ X-ray tomography analysis of the evolution of pores during deformation of AlSi10Mg fabricated by selective laser melting, Mater. Lett. 255 (2019) 126512.

[8] J. Samei, M. Amirmaleki, A.P. Ventura, G.T. Pawlikowski, M. Bayes, W.Z. Misiolek, D.S. Wilkinson, In-situ X-ray tomography analysis of the evolution of pores during deformation of a Cu-Sn alloy fabricated by selective laser melting, Addit. Manuf. 34 (2020) 101196.

[9] J. Samei, A. Sadeghi, H. Mortezapour, S. Salavati, M. Amirmaleki, M. Pekguleryuz, D.S. Wilkinson, 4D X-ray tomography characterization of void nucleation and growth during deformation of strontium-added AZ31 alloys, Mater. Sci. Eng.: A 797 (2020) 140081.

[10] W. Yashiro, D. Noda, K. Kajiwara, Sub-10-ms X-ray tomography using a grating interferometer, Appl. Phys. Express 10 (5) (2017).

[11] X. Liang, W. Voegeli, H. Kudo, E. Arakawa, T. Shirasawa, K. Kajiwara, T. Abukawa, W. Yashiro, Sub-millisecond 4D X-ray tomography achieved with a multibeam X-ray imaging system, Appl. Phys. Express 16 (7) (2023).

[12] F. García-Moreno, P.H. Kamm, T.R. Neu, F. Bülk, M.A. Noack, M. Wegener, N. von der Eltz, C.M. Schlepütz, M. Stampanoni, J. Banhart, Tomoscopy: Time-resolved tomography for dynamic processes in materials, Adv. Mater. 33 (45) (2021) 2104659.

[13] C. Jailin, A. Bouterf, M. Poncelet, S. Roux, In situ micro CT-scan mechanical tests: Fast 4D mechanical identification, Exp. Mech. 57 (2017) 1327–1340.

[14] Y. Gao, J. Smith, P. Lee, Tracking damage evolution in additively manufactured AlSi10Mg using in situ X-ray computed tomography, Acta Mater. 237 (2023) 118136.

[15] B. Müller, H. Deyhle, S. Lang, G. Schulz, T. Bormann, F.C. Fierz, S.E. Hieber, Three-dimensional registration of tomography data for quantification in biomaterials science, Int. J. Mater. Res. 103 (2) (2012) 242–249.

[16] Y. Lei, Y. Fu, T. Wang, Y. Liu, P. Patel, W.J. Curran, T. Liu, X. Yang, 4D-CT deformable image registration using multiscale unsupervised deep learning, Phys. Med. Biol. 65 (8) (2020) 085003.

[17] O. Kafka, A. Landauer, J. Benzing, N. Moser, E. Mansfield, E. Garboczi, A technique for in-situ displacement and strain measurement with laboratory-scale X-Ray computed tomography, Exp. Tech. 48 (2024) 1101–1116.

[18] E. Zwanenburg, M. Williams, J. Warnett, Review of high-speed imaging with lab-based X-ray computed tomography, Meas. Sci. Technol. 33 (2021).

[19] Deep learning reconstruction of few-view X-ray CT measurements of mono-material objects with validation in additive manufacturing, CIRP Ann 73 (2024) 381–384.

[20] A. Ziabari, S.V. Venkatakrishnan, Z. Snow, A. Lisovich, M. Sprayberry, P. Brackman, C. Frederick, P. Bhattad, S. Graham, P. Bingham, R. Dehoff, A. Plotkowski, V. Paquit, Enabling rapid X-ray CT characterisation for additive manufacturing using CAD models and deep learning-based reconstruction, Npj Comput. Mater. (2023).

[21] H.A. Ali, E.A. Rashed, H. Kudo, Compressed sensing-based image reconstruction for discrete tomography with sparse view and limited angle geometries, PLoS One 20 (7) (2025) Published: July 11, 2025.

[22] J. Lehtinen, J. Munkberg, J. Hasselgren, S. Laine, T. Karras, M. Aittala, T. Aila, Noise2Noise: Learning image restoration without clean data, 2018.

[23] M. Andrew, A. Andreyev, F. Yang, M. Xu, S. Xu, X-ray reconstruction using synthetic prior image restoration, with application to noise and artefact removal, Dev. X-Ray Tomogr. XV Proc. 13152 (2024).

[24] Y. Zhang, Z. Yao, R. Klöfkorn, et al., 4D-ONIX for reconstructing 3D movies from sparse X-ray projections via deep learning, Nat. Commun. Eng. 4 (54) (2025).

[25] D.S. Watring, K.C. Carter, D. Crouse, B. Raeymaekers, A.D. Spear, Mechanisms driving high-cycle fatigue life of as-built inconel 718 processed by laser powder bed fusion, Mater. Sci. Eng. A 761 (2019).

[26] Deben U.K. Ltd., CT5000 tensile stage for X-ray CT tomography, 2024, n.d. https://deben.co.uk/tensile-testing/%C2%B5xct/tensile-stages-for-x-ray-ct-tomography/. (Accessed 23 April 2025).

[27] L.A. Feldkamp, L.C. Davis, J.W. Kress, Practical cone-beam algorithm, J. Opt. Soc. Amer. A 1 (6) (1984) 612–619.

[28] V.V.R. Bukka, M. Xu, M. Andrew, A. Andreyev, Assessment of deep-learning-based resolution recovery algorithm relative to imaging system resolution and feature size, Methods Microsc. (2025).

[29] H. Villarraga-Gómez, P. Brackman, A. Ziabari, O. Rahman, Z. Snow, R. Shahani, K. Bugelnig, A. Andreyev, Y. Trenikhina, N. Johnson, H. Bale, J. Schulz, E.C. Santos, Multiscale characterization of additive manufacturing components with computed tomography, 3D X-ray microscopy, and deep learning, J. Nondestruct. Eval. 44 (2025) 110.

[30] Carl Zeiss Research Microscopy Solutions, Advanced reconstruction toolbox 4.0, 2025, n.d. https://www.zeiss.com/microscopy/us/products/software/advanced-reconstruction-toolbox.html. (Accessed 23 April 2025).

[31] Z. Wang, A. Bovik, H. Sheikh, E. Simoncelli, Image quality assessment: from error visibility to structural similarity, IEEE Trans. Image Process. 13 (4) (2004) 600–612.

[32] C.Z.X. ray Microscopy, Deeprecon pro user manual, 2025, (Accessed 23 April 2025).

[33] N. Moser, A. Landauer, K. O.L., IMPPY3D: Image processing in python for 3D image stacks, J. Open Source Softw. 10 (2025).

[34] R. Beare, B. Lowekamp, Z. Yaniv, Image segmentation, registration and characterization in r with simpleitk, J. Stat. Softw. 86 (2018).

[35] Z. Yaniv, B.C. Lowekamp, H.J. Johnson, R. Beare, SimpleITK image-analysis notebooks: a collaborative environment for education and reproducible research, J. Digit. Imaging 31 (2018) 290–303.

[36] B.C. Lowekamp, D.T. Chen, L. Ibáñez, D. Blezek, The design of SimpleITK, Front. Neuroinform. 7 (2013).

[37] S. Van der Walt, J.L. Schönberger, J. Nunez-Iglesias, F. Boulogne, J.D. Warner, N. Yager, E. Gouillart, T. Yu, Scikit-image: image processing in python, PeerJ 2 (2014) e453.

[38] C.R. Harris, K.J. Millman, S.J. van der Walt, R. Gommers, P. Virtanen, D. Cournapeau, E. Wieser, J. Taylor, S. Berg, N.J. Smith, R. Kern, M. Picus, S. Hoyer, M.H. van Kerkwijk, M. Brett, A. Haldane, J.F. del Río, M. Wiebe, P. Peterson, P. Gérard-Marchant, K. Sheppard, T. Reddy, W. Weckesser, H. Abbasi, C. Gohlke, T.E. Oliphant, Array programming with numpy, Nature 585 (7825) (2020) 357–362.

[39] N. Otsu, et al., A threshold selection method from gray-level histograms, Automatica 11 (285–296) (1975) 23–27.

[40] E. Hosseini, V. Popovich, A review of mechanical properties of additively manufactured inconel 718, Addit. Manuf. 30 (2019) 100877.

[41] A. du Plessis, S.G. le Roux, G. Booysen, J. Els, Directionality of cavities and porosity formation in powder-bed laser additive manufacturing of metal components investigated using X-Ray tomography, 3D Printing and Additive Manufacturing, vol. 3 (1) (2016) 48–55.

[42] A. du Plessis, P. Sperling, A. Beerlink, L. Tshabalala, S. Hoosain, N. Mathe, S.G. le Roux, Standard method for microct-based additive manufacturing quality control 2: Density measurement, MethodsX 5 (2018) 1117–1123.

[43] F. Kim, S. Moylan, E. Garboczi, J. Slotwinski, Investigation of pore structure in cobalt chrome additively manufactured parts using X-ray computed tomography and three-dimensional image analysis, Addit. Manuf. 17 (2017) 23–38.

[44] H. Gong, V.K. Nadimpalli, K. Rafi, T. Starr, B. Stucker, Micro-CT evaluation of defects in Ti-6Al-4V parts fabricated by metal additive manufacturing, Technologies 7 (2) (2019).

[45] I. Holgado, N. Ortega, J.A. Yagüe-Fabra, S. Plaza, H. Villarraga-Gómez, Metrological evaluation and classification of porosity in metal additive manufacturing using X-ray computed tomography, Mater. Des. 254 (2025) 114057.